Journal of Catalysis 438 (2024) 115722

Contents lists available at ScienceDirect

Journal of Catalysis

journal homepage: www.elsevier.com/locate/jcat

Partial oxidation of cyclohexene over histidine-modified Cu-UiO-66 under aerobic conditions

Erlend Aunan [a], Valeria Finelli [b,c], Sebastian Prodinger [a,*], Ning Cao [a,d], Beatrice Garetto [b], Gabriele Deplano [b], Peter Ng'ang'a Njoroge [a], Matteo Signorile [b], Elisa Borfecchia [b], Karl Petter Lillerud [a], Ainara Nova [a,d], Silvia Bordiga [b,*], Unni Olsbye [a,*]

[a] SMN Centre for Material Science and Nanotechnology, Department of Chemistry, University of Oslo, N-0315 Oslo, Norway
[b] Department of Chemistry, NIS and INSTM Reference Centre, Università di Torino, Via G. Quarello 15/A, I-10135, and Via P. Giuria 7, I-10125, Turin, Italy
[c] University School for Advanced Studies, IUSS Pavia, Palazzo del Broletto, Piazza Della Vittoria 15, I-27100, Pavia, Italy
[d] Hylleraas Centre for Quantum Molecular Sciences, Department of Chemistry, University of Oslo, P. O. Box 1033, Blindern, N-0315 Oslo, Norway

ARTICLE INFO

Keywords:
Post-synthetic functionalization
MOF
UiO-66
Cyclohexene oxidation
Cu
Histidine
LPMO
Bio-inspired

ABSTRACT

Enzyme-inspired catalysis is an attractive approach for developing selective hydrocarbon partial oxidation processes. Here, histidine was introduced into defective UiO-66 metal–organic framework by ligand exchange, followed by Cu(II) ion insertion. Density functional theory modeling combined with X-ray Absorption spectroscopy revealed that Cu(II) has a higher affinity for open Zr-O node sites than for histidine, leading to a series of materials where Cu(II) ions are predominantly anchored to the $Zr_6O_4(OH)_4$ nodes, while only minority fractions of Cu(II) are anchored to histidine. Catalytic testing for aerobic cyclohexene oxidation with *tert*-butyl hydroperoxide (t-BuOOH) in trifluorotoluene solution at 25 °C showed activity for cyclohexene oxidation to cyclohexenol and cyclohexenone, with high selectivity. Benchmark tests revealed that Cu and t-BuOOH are both essential for the reaction, yet t-BuOOH consumption was far inferior to product formation rates, suggesting a radical reaction pathway involving O_2.

1. Introduction

Bio-inspired catalysis is an emerging field of research, aiming for the specificity and selectivity of enzymatic catalysts while excluding their extensive peptide structure. The ability of cuproenzymes such as particulate methane monooxygenase (pMMO) and lytic polysaccharide monooxygenases (LPMOs) to achieve the partial oxidation of strong C—H bonds at ambient conditions [1,2] has inspired researchers to explore mono-Cu complex catalysts for a variety of partial oxidation reactions [3–5].

Focusing here on LPMO enzymes, their active motif consists of a mono-copper ion coordinated to two histidine residues, often referred to as the histidine-brace (Fig. 1) [6]. LPMOs activate strong C—H bonds in crystalline polysaccharides (estimated to be 397–435 kJ/mol [7]), leading to the cleavage of glycosidic bonds and the formation of one normal and one oxidized new chain end. It is debated whether LPMO is mainly a mono- or per-oxygenase [2]. In support of a peroxygenase-dominated mechanism, recent studies on LPMOs revealed that the rate of reaction between LPMOs and H_2O_2 is orders of magnitude faster than its reaction with O_2 [2,8,9].

Among test reactions for bio-inspired Cu catalysts, the partial oxidation of cyclohexene is among the most studied ones, due to the industrial interest in the production of cyclohexene oxide and cyclohexanol, [11] and possibly also because the weaker allylic C—H bonds of cyclohexene (343 kJ/mol) [12] compared to the C—H bonds in alkanes such as cyclohexane (427 kJ/mol) [12] makes it an easier target. When conducted without a catalyst at elevated temperatures (70–120 °C), a radical chain reaction between cyclohexene and O_2 yields cyclohexenyl hydroperoxide as primary product, followed by autocatalytic production of cyclohexenol, cyclohexenone, and cyclohexene oxide, with apparent activation energies in the range 86–108 kJ/mol [11]. Fifty years ago, Ikamura *et al.* tested a Cu-Cl complex as a cyclohexene oxidation catalyst in acetic acid at 60 °C and reported the conversion of cyclohexene and O_2 to cyclohexenyl hydroperoxide as a primary

* Corresponding authors.
E-mail addresses: Sebastian.Prodinger@smn.uio.no, SEPR@topsoe.com (S. Prodinger), silvia.bordiga@unito.it (S. Bordiga), unni.olsbye@kjemi.uio.no (U. Olsbye).

https://doi.org/10.1016/j.jcat.2024.115722
Received 3 June 2024; Received in revised form 8 August 2024; Accepted 12 August 2024
Available online 22 August 2024

product, followed by its partial decomposition to cyclohexenone and cyclohexenol, in line with results obtained in uncatalyzed systems. The addition of LiCl salt enhanced the rates of hydroperoxide formation as well as hydroperoxide decomposition [13]. Later, several catalyst motifs in which Cu is coordinated to N, O, or both, have been synthesized and tested for cyclohexene oxidation, using O_2, H_2O_2, or *tert*-butyl hydroperoxide (t-BuOOH) as oxidant, in homogeneous systems and after immobilization in zeolites, silica, alumina, polymers or metal–organic frameworks. Cyclohexenyl hydroperoxide, cyclohexenone, and cyclohexenol are reported as the main products in some studies, while cyclohexene oxide and its hydrolysis product, cyclohexane-1,2-diol, are the main products in other studies. (See *e.g.* refs [14–27]). Some papers reported the addition of a radical scavenger to the reaction mixture. Quenching of the reaction was observed in all cases, leading the authors to conclude that cyclohexene oxidation proceeded *via* a radical chain reaction [24,28,29]. A mechanistic proposal based on literature reports on Cu-catalyzed cyclohexene/t-BuOOH conversion under aerobic conditions, is presented in Scheme 1. Referring to the different product selectivities observed for various catalysts, it may depend on the ability of each catalyst to promote reaction steps beyond the initial formation of radicals or suggest a parallel, non-radical route.

Considering the LPMO motif (Fig. 1), it becomes evident that the interaction between histidine and copper might hold the key to enabling monooxygenase activity under normal temperature and pressure conditions. Weckhuysen *et al.* reported studies of a system consisting of a histidine-based Cu complex, Cu(histidine)$_2$, inserted into FAU zeolite. Testing of cyclohexene oxidation with t-BuOOH at 60 °C without solvent, led predominantly to the formation of cyclohexene oxide and its hydrolysis product, 1,2-cyclohexanediol (a total of 98 % selectivity). Only minor amounts of cyclohexenol and cyclohexenone were formed [14,15].

Histidine was recently incorporated with Cu in a Zr-based metal–organic framework, MOF-808, and tested for partial oxidation of methane in a chemical looping mode at 150 °C [34]. The reported catalytic motif consists of a Cu_2O_2 dimer coordinated to the imidazole rings of two histidine ligands. A maximum of 1.3 % stoichiometric productivity per Cu site was reported.

Among Zr-based MOFs, UiO-66 ($Zr_6(\mu_3\text{-}O)_4(\mu_3\text{-}OH)_4(BDC)_6$, BDC: 1,4-benzenedicarboxylate) is recognized as one of the archetypical metal–organic frameworks, due to its exceptional physicochemical stability, [35–38] attributed to the robust twelve-coordination interaction between Zr^{4+} ions and carboxylate groups within the secondary building units (SBUs) and terephthalate linkers. Because of these attributes, UiO-66 is a prime candidate as catalyst support for heterogeneous catalysts.

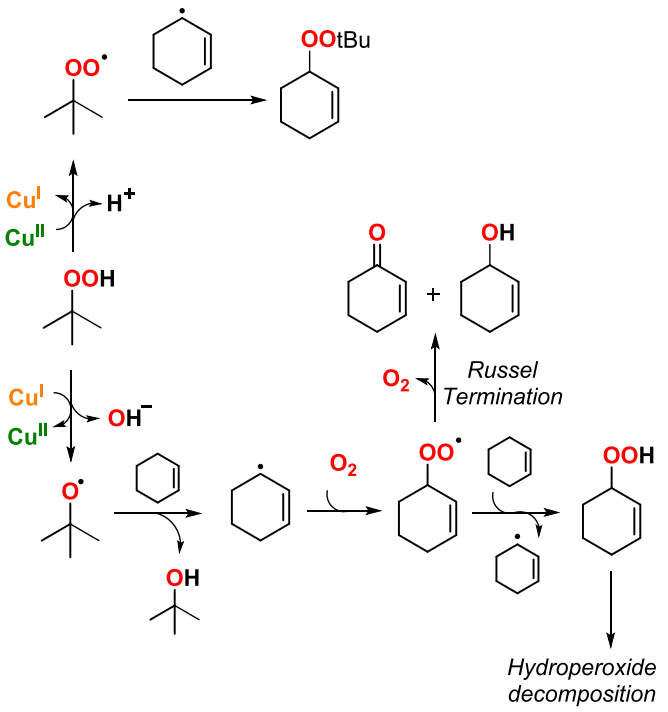

Scheme 1. Proposed reaction pathways for cyclohexene oxidation in the presence of t-BuOOH and O_2. The Scheme represents a combination of mechanistic information from refs[30–33].

In later years, open coordination sites between two Zr_6-SBUs – known as missing linker defects – have been shown to offer a highly exploitable route for post-synthetic functionalization [39–41]. After synthesis, these open coordination sites are typically populated by monodentate ligands which are remnants from the synthesis mixture, such as formate (from *N*, *N*-dimethylformamide hydrolysis), acetate from acetic acid used as a modulator, or water/hydroxide pairs. Such ligands are typically quite labile and can be replaced with others using solvent-assisted ligand exchange (SALE) [34,39,42].

In this contribution, we introduced histidine into linker-defective UiO-66 using the SALE approach, to establish bio-inspired anchor points that may facilitate the ligation of copper. The materials obtained were characterized by standard methods such as N_2 physisorption, powder X-ray diffraction, liquid state NMR, atomic emission

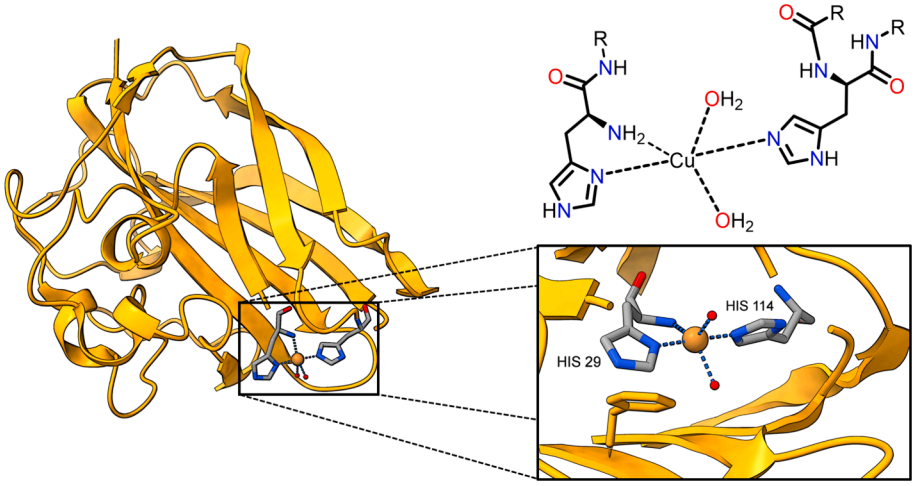

Fig. 1. Lytic polysaccharide monooxygenase (LPMO), with its cofactor Cu, N_3-coordinated to two histidines forming the so-called "histidine brace". PDB reference code: 4alc[10].

spectrometry, FT-IR, as well as DFT-assisted XAS analysis; and tested for cyclohexene oxidation at 25 °C with t-BuOOH in trifluorotoluene solvent, under aerobic conditions. Computational results suggest that Cu attachment to open Zr-node sites is thermodynamically more favorable than to histidine, in line with experimental characterization of the materials. The materials showed activity for cyclohexene oxidation to cyclohexenol and cyclohexenone, with high selectivity. The reaction was initiated by Cu – t-BuOOH interaction, followed primarily by a radical reaction pathway.

2. Results and discussion

2.1. Materials synthesis

Detailed synthesis procedures are presented in **Supporting Information, Section S2**. UiO-66 was synthesized at low reaction temperatures (90 °C) to facilitate high linker defectivity in the obtained product. Cu K-edge X-ray absorption spectroscopy is a key technique to elucidate the copper environment, and because of a partial overlap between the EXAFS region of the Cu K-edge (8979 eV) and the Hf L_3 edge (9561 eV), it was of utmost importance to limit the concentration of hafnium in the samples. Hafnium is a common impurity found in most zirconium sources, due to their chemical similarities [43]. Hence, a low-Hf zirconium precursor (zirconyl chloride hydrate) was synthesized from a low-Hf containing batch of $ZrCl_4$ [44]. (See ESI for more details).

The obtained parent material, hereafter called "UiO-66", was then reacted with an excess of histidine in water, at 60 °C. The saturated histidine solution was not pH-adjusted from its pH of 8, as it was found that lowering the pH was detrimental to the degree of incorporation (**Supporting Information**, **Figure S1**). Further increase of pH was not attempted as higher pH values are known to be harmful to UiO-66 [45]. By varying the histidine concentration, materials with different histidine contents were obtained. Initially, a pair of daughter materials which originate from the same batch of UiO-66 was synthesized. The yielded materials, dubbed His-1 and His-2, were then metalated using Cu $(BF_4)_2{\cdot}xH_2O$ in acetonitrile at room temperature. The metalation gives His-Cu-1 and His-Cu-2, respectively. To ensure enough material for catalytic testing purposes, a third batch was synthesized using commercial-grade zirconyl chloride. This third batch, which yielded a material which is referred to as His-Cu-3, was therefore not characterized to the same extent as the paired materials His-Cu-1 and His-Cu-2. An overview of all the synthesized samples is shown in Table 1.

2.2. Basic characterization of the synthesized materials

Basic characterization of parent UiO-66, histidine- and copper-loaded samples are presented in **ESI, Section S3** (**Figures S2-S17 and Tables S2-S3**). Powder diffractograms (**Figure S2**) show the expected UiO-66 **fcu**-phase, with the addition of two broad, forbidden peaks at low diffraction angles. These peaks reveal the presence of a **reo**-phase in the material, commonly referred to as missing-cluster defects. Although not quantified, the relative intensities of the (100) and (110) reflections, visible at $2\theta = 4.3°$ and 6.1° respectively, suggest a substantial amount of **reo**-nanoregions present in the parent material [46,47. The powder diffractograms appear unchanged across the synthetic steps, which indicates that the functionalized materials retain their crystallinity after each treatment, which is also evident from the retention of the surface area, measured by isothermal N_2 adsorption at 77 K (**Figure S7**). The presence of the more open **reo**-phase is likely contributing to an increased surface area, as the surface area of the parent material (1693 m^2g^{-1}) is higher than what is usually reported for UiO-66 [38,47]. It is worth pointing out the lack of the **reo**-phase in the independent sample (Cu-His-3). This is apparent in the powder X-ray diffractogram as well as in the nitrogen adsorption behavior of the sample.

Thermogravimetric analysis performed in synthetic air (**Figure S13**) reveals a noticeable, but predictable decrease in thermal stability for each post-synthetic step; firstly, as formate and acetate are replaced by the less thermally stable histidine molecule, and secondly as copper is introduced – potentially catalyzing the decomposition of the MOF.

DRS-UV Visible spectra, collected on the His-1 and His-2-based samples at each preparation step, testify that sample modifications occurred upon histidine and Cu insertion. In **Figure S19** the spectrum of Parent UiO-66 is characterized by a strong absorption in the UV region (starting from 32500 cm^{-1}) that can be ascribed to π-π* transition of the terephthalate (BDC) linker [48]. The inclusion of histidine slightly modifies the spectral profile of the original material, showing a weak contribution at ca. 30000 cm^{-1}. Also, the reflectance of this latter band decreases for the Cu-containing materials, where an additional weaker signal near 26000 cm^{-1} appears still in the charge transfer region. The presence of Cu(II) is qualitatively confirmed by the band in the d-d region visible at around 14000 cm^{-1}. This feature is very broad, suggesting a heterogeneity of the copper environments in the two samples.

Histidine exchange was confirmed and quantified using ^1H NMR spectroscopy on digested samples of the material. Due to the paramagnetic nature of Cu(II) centers, quantification of histidine was not possible after metalation. We assume the histidine content to remain constant after copper insertion, due to histidine's insolubility in acetonitrile [49]. The absence of strongly colored copper histidinate complexes in the washings also supports the assumption [50]. The relative ratios of defect-terminating ligands (histidine, formate, and acetate) to linker (terephthalic acid) were measured and used in tandem with the observed mass-loss in the thermogram which gives the mass ratio of organic to inorganic species present in the MOF. This allows for the estimation of the chemical composition of the obtained products [51]. As observed from Table 1, the Cu/his ratios in the three materials were 2.6, 7.0, and 1.8, respectively, suggesting either that Cu was present as Cu clusters, or that individual Cu ions were mainly attached to other sites than histidine. From these two possibilities, DFT calculations and EXAFS analysis (see below) support the location of individual Cu ions on the Zr-node.

Table 1
Overview of the materials discussed in this work.

Name	Sample	Estimated composition per $[Zr_6O_4(OH)_4]^{12+}$					Cu:His	Surface area†	Pore volume‡
		BDC	OAc	$[OH+H_2O]^-$	His	Cu		$[m^2g^{-1}]$	$[cm^3g^{-1}]$
UiO-66	Defective UiO-66	4.6	0.5	2.3	–	–	–	1694	0.67
His-1	UiO-66-$his_{0.31}$	4.3	0	3.1	0.31	–	–	1563	0.65
His-2	UiO-66-$his_{0.08}$	4.3	0.1	3.3	0.08	–	–	1677	0.68
His-Cu-1	UiO-66-$his_{0.31}Cu_{0.81}$	4.3	0	3.1	0.31	0.81	2.6	1507	0.64
His-Cu-2	UiO-66-$his_{0.08}Cu_{0.56}$	4.3	0.1	3.3	0.08	0.56	7	1725	0.71
His-Cu-3ǂ	UiO-66-$his_{0.42}Cu_{0.77}$	4.5	0	2.6	0.42	0.77	1.8	1073	0.46

† : Specific surface area as measured with BET, using N_2 adsorption at 77 K.
‡ : Pore volume measured at $p/p_0 = 0.8$, using N_2 adsorption at 77 K.
ǂ : Batch made with a different parent for the sake of catalytic testing.

2.3. Density functional theory based characterization

Overall, the elemental analysis data presented in Table 1 suggest that histidine attaches to the Zr-node, partially occupying missing linker defects, while Cu interacts both with histidine and the Zr-node. To corroborate this hypothesis, DFT calculations were used to obtain structural information on the Cu-sites and their energy. Three different models were built using periodic calculations, starting from the optimized structure of the pristine UiO-66 [52] using PBE-D3/DZVP (see **ESI, Section S5** for details). This step was followed by the replacement of a linker by either histidine (**Zr-His**), a neutral hydrated Cu(II) species (**Zr-Cu**), or a histidine-Cu(OH) complex (**Zr-His-Cu**). Preliminary EXAFS analysis (*vide infra*) indicated that the coordination number of the Cu ions attached to the Zr-node is at least five, while it is four for the Cu attached to histidine. This information was also used to build the periodic models, which were fully optimized (Fig. 2A–C). In addition to the structures shown in Fig. 2, other conformations, coordination numbers, and charged species were considered (see **ESI section 5**). However, they gave either slightly higher energy or a worse fit with EXAFS.

We first consider the periodic models in Fig. 2. As Fig. 2A illustrates, the imidazole ring of histidine in **Zr-His** can interact *via* hydrogen bonding with Zr-OH groups resulting from the missing linker defect, with NH-O distances of 2.25 Å. In **Zr-His-Cu,** the nitrogen of the amine (N_{amine}), the imidazole (N_{IM}), and two hydroxyls formed a tetra-coordinated copper configuration. Two nitrogen atoms from the histidine coordinated with the copper atom exhibit Cu-N bond distances of 1.99 Å and 2.14 Å. The bond distances between Cu and the OH groups are 1.91 Å and 2.00 Å, respectively. For **Zr-Cu,** penta- and hexa-coordinated Cu centers at the defective sites were modeled (**ESI, Figure S20**). In the penta-coordinated structures, Cu is bound to three hydroxyl groups and two water molecules in a square pyramid configuration. Remarkably, Cu-OH_2 distances vary significantly depending on their orientation towards different cavities. For instance, Cu-OH_2 bond lengths were 2.30 Å and 2.32 Å when H_2O occupied the octahedral cavity, and 2.07 Å and 2.70 Å in the tetrahedral cavity.

In addition to the periodic structures, cluster models were built to re-evaluate distances (Fig. 2). To mimic the cage effect of the MOFs, four neighboring linkers were retained. Additionally, we simulated the structural rigidity of UiO-66 by imposing constraints on the positions of the oxygen atoms at the carboxylate sites and the Zr atoms at the Zr nodes. Cluster models derived from periodic structures were further optimized using PBE0-D3(BJ)/def2-SVP method, which led to small changes in the Cu–O, Cu–N distances ($\Delta d < 0.1$ Å except for Cu-OH_2 0.17 Å). These optimized structures were validated against the available EXAFS experimental spectra (*vide infra*).

2.4. X-ray absorption spectroscopy

2.4.1. Qualitative overview of the as-prepared materials using XANES and FT-EXAFS

Two UiO-66-his-Cu MOFs, His-Cu-1 and His-Cu-2, with different histidine and Cu loading (see Table 1), were characterized by Cu K-edge XAS in their as-prepared state. In Fig. 3, spectra collected in inert conditions at RT of the two samples are compared in both XANES (Fig. 3A) and FT-EXAFS (Fig. 3B) regions.

As expected, the XANES spectra exhibit the characteristic spectral

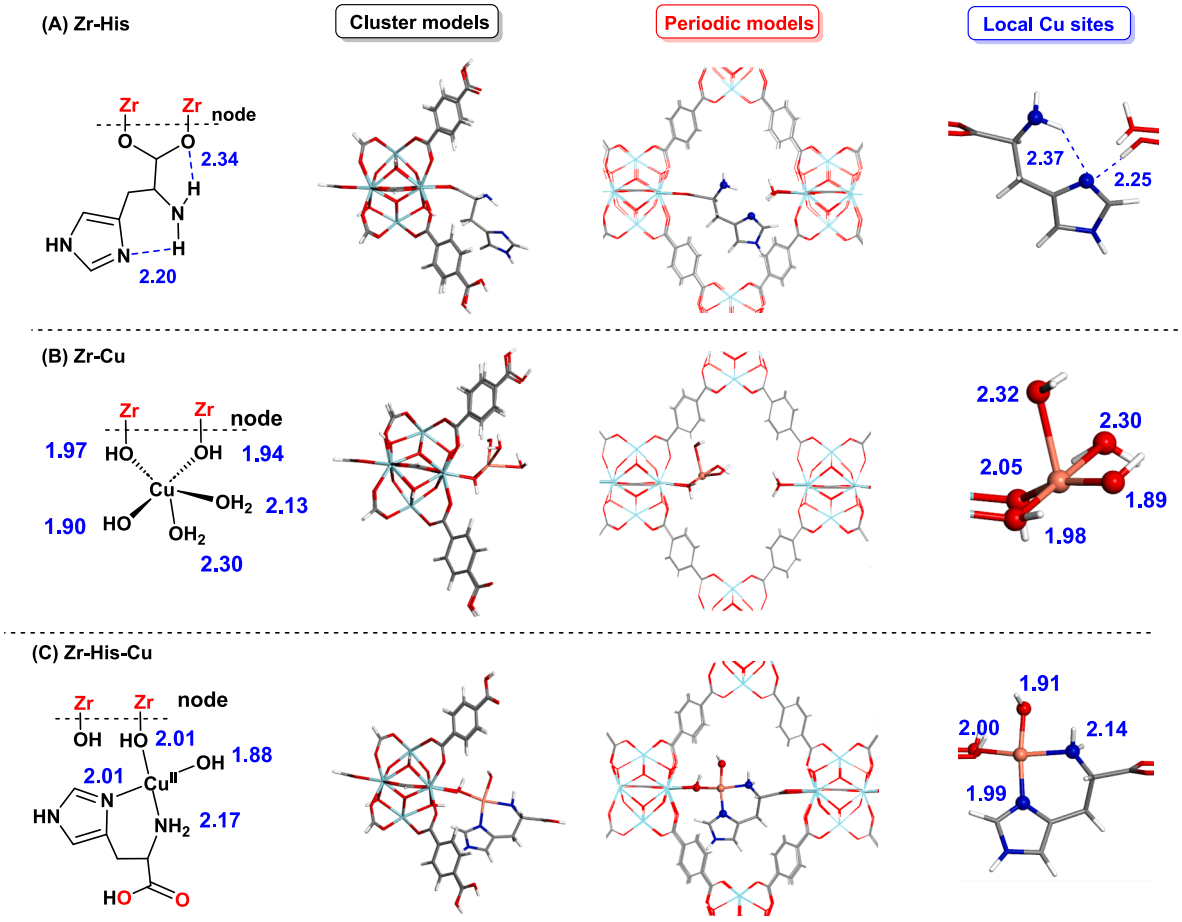

Fig. 2. Optimized geometries using cluster and periodic models for the Zr-His (A), Zr-Cu (B), Zr-His-Cu (C) structures. Bond distances obtained with the cluster models are labeled in blue and frozen atoms in red. Periodic models and their local copper sites are displayed. (For interpretation of the references to color in this figure legend, the reader is referred to the web version of this article.)

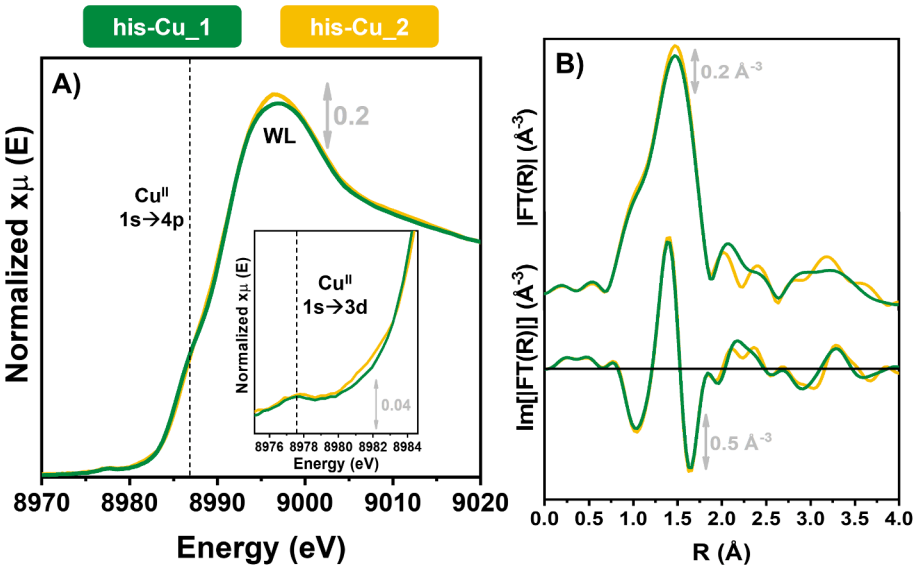

Fig. 3. (**A**) XANES spectra representation of His-Cu-1 and His-Cu-2 samples. Additionally, a magnification of the Cu(II) 1 s→3d pre-edge peak is also reported. (**B**) Phase-uncorrected magnitude FT-EXAFS spectra of the examined samples are depicted on the top, while the imaginary FT-EXAFS spectra are presented on the bottom.

features associated with the Cu(II) oxidation state. While the intensity of the white line (WL) peak indicates, on average, a 5/6-coordinated Cu(II) site in both samples, subtle variations in its shape and intensity can suggest potential differences in the average Cu(II) coordination geometry, and thus Cu-speciation. Notably, the Cu(II) 1s→4p transition peak is slightly more pronounced in His-Cu-1 (the highest histidine and Cu loading sample), underscoring structural distinctions between the two samples.

Upon closer examination of the FT-EXAFS spectra, minor differences emerge, particularly in correspondence with the second and third coordination shell peak of the absorber (Fig. 3B, top spectrum). Furthermore, the imaginary FT-EXAFS plot (Fig. 3B, bottom spectrum) reveals a well-defined oscillation at approximately 3.3 Å. This feature may be attributed to the presence of a heavy-atom scatterer, tentatively associated with a Cu-Cu or Cu-Zr single scattering contribution.

Considering these observations, we qualitatively confirm that the two as-prepared MOFs can be defined as distinct materials, a classification supported by their post-synthesis composition reported in Table 1.

2.4.2. *Validation of local structure and Cu speciation by DFT-assisted EXAFS fitting*

EXAFS fit analysis was conducted to quantitatively corroborate the differences previously identified qualitatively between His-Cu-1 and His-Cu-2. Fig. 4 summarizes the DFT-optimized structures and the results derived from fitting the experimental spectrum collected at RT under inert conditions (He gas feed) for both samples.

Focusing on the compositional differences of the two proposed samples, especially on the amount of histidine present within the systems, different approaches to the analysis were considered. In the first

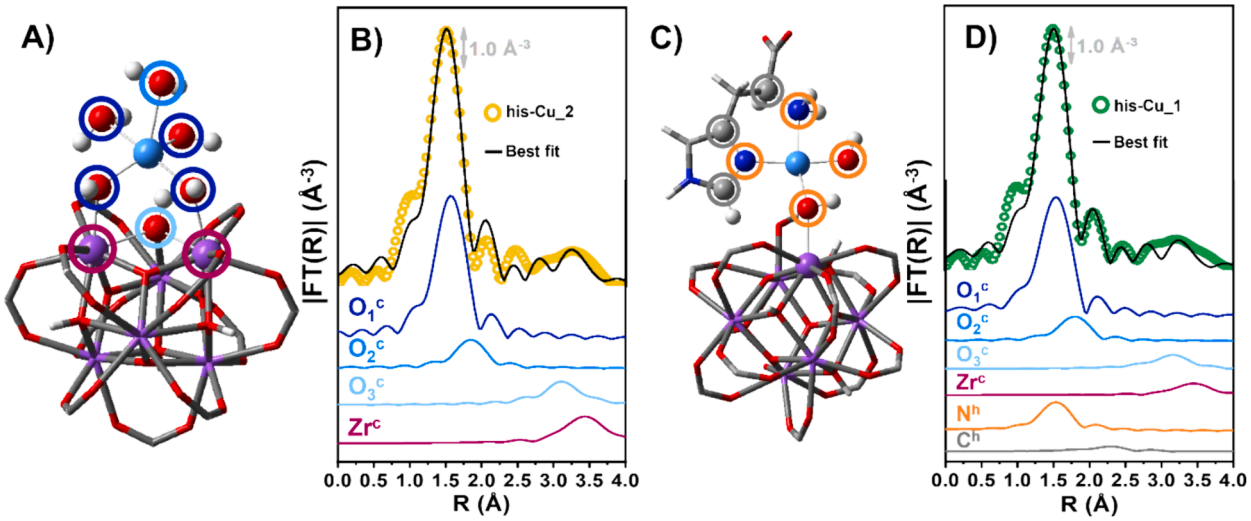

Fig. 4. (**A**,**C**) Magnification of Cu(II) site on the Zr node, Zr-Cu (A) and Cu(II) site coordinated to histidine, Zr-His-Cu (C), highlighting the different scattering contributions considered in the fit analysis by colored circles, using the same color code as in part (B,D). (**B**,**D**) Phase-uncorrected modulus of experimental and best fit FT-EXAFS spectra for His-Cu-2 (B) and His-Cu-1 (D) samples at RT in He. The experimental data are shown as colored open circles and the best fits with black solid lines. The principal SS contributions included in the fitting model are reported as colored solid lines, vertically translated for the sake of clarity. Here, the 'c' superscript indicates contributions from Zr-Cu species, while the 'h' superscripts indicate contributions from Zr-His-Cu.

approach, the Zr-Cu model, describing Cu(II) ions located in defective Zr cluster sites (indicated hereafter with the ^{c} superscript) shown in Fig. 4A, is used as the initial model for the His-Cu-2 (UiO-66-his$_{0.08}$Cu$_{0.56}$) EXAFS spectrum. Remarkably, the analysis yielded an excellent reproduction of the experimental spectrum, demonstrated by an R factor of less than 1 % and the attainment of physically reliable values for all optimized parameters in the fit (see **Table S5 in ESI**). The FT-EXAFS spectrum reported in Fig. 4B (top) is successfully reproduced considering a more symmetric first coordination sphere, contributing at an average distance of (1.941 ± 0.009) Å for O_1^c. The Cu coordination environment is completed by the contribution of O_2^c, belonging to a farther H_2O extra-ligand molecule at (2.24 ± 0.03) Å. Although the EXAFS-optimized model shows some slight rearrangements concerning the DFT one, this latter Cu-OH_2 distance falls closer to the DFT predictions when H_2O occupies the octahedral cavity. Hence, EXAFS analysis suggests that this is the preferred/more probable configuration, although other options cannot be ruled out due to the absorber-average nature of the XAS technique.

Upon closer examination of the principal SS contributions incorporated in the fitting model (Fig. 4B, bottom), it became evident that the signal originating from the second coordination shell is also attributed to O_2^c. In the high-R range, a broad but detectable peak is visible and identified as SS contributions from more distant O_3^c and Zr atoms, which is consistent with the preferential location of Cu(II) species on the defective Zr node. Notably, the reproduction of this signal is good but not perfect, since the MS paths contributing to this range were omitted from the analysis and detecting scattering contributions from more distant atoms (R>3.5 Å) proved to be challenging.

In conclusion, the outcomes derived from the fitting process unequivocally validate our initial hypothesis indicating that copper is located on the defective nodes in His-Cu-2.

Meanwhile, the second approach involves the two-component EXAFS-fit analysis (for further details on the specific method, refer to **ESI Section 6.1**) on the His-Cu-1 (UiO-66-his$_{0.31}$Cu$_{0.81}$) sample. The rationale behind opting for this analytical approach stemmed from the intention to ascertain whether the two proposed materials display distinct characteristics and Cu-speciation. Specifically, the tendency of histidine to integrate into the defective sites of the Zr node, as well as its capability to further coordinate Cu ions, was assessed. In Fig. 4C, the optimized Zr-His-Cu DFT structure depicting the Cu(II) site coordinated to histidine (indicated hereafter with ^{h} superscript) is illustrated, while Fig. 4D reports the associated fit outcomes.

In the comprehensive analysis of the EXAFS fit results reported in Fig. 4D, a good agreement between the experimental spectrum and the best-fit curve is evident. A careful examination of the SS path contributions reveals that the first-shell peak is distinctly described by O_1^c and O_2^c atoms coming from the defective node model (Fig. 4D), in conjunction with N^h atoms associated with the Cu(II)-histidine structure (Fig. 4C). Notably, the first coordination shell in the Cu(II)-histidine structural model is explicitly constituted by two N atoms belonging to the histidine molecule, complemented by two O atoms from the MOF node and an OH extra-ligand. The fitting outcomes underscore a more symmetric Cu(II) coordination environment; hence all constituent atoms are defined using an analogous N^h parametrization with an average interatomic distance of 2.00 ± 0.04 Å.

The characteristics of the second shell are effectively reproduced considering the collective contributions by O_3^c and Zr^c, albeit with a modest yet detectable contribution from the C^h histidine atoms. Interestingly, the absence of SS contributions from Zr within the Cu(II)-histidine structure validates a more distant Cu(II) from the MOF metal node. Regrettably, the broad features inherent to the third coordination shell cannot be described precisely due to the non-inclusion of MS paths.

Nonetheless, explicit differences in the SS paths contribution intensities are visible. It is discerned, in this context, that the Cu(II)-histidine structural component manifests relatively subdued contributions, suggesting predominant Cu(II) defective node sites in this sample. According to these fitting results, the experimental data rigorously validate our qualitative hypotheses, proving the coexistence of distinct Cu(II) sites. Best-fit values for the parameters optimized in the two-component EXAFS fit, referring to the Zr-His-Cu structure, are reported in **Table S4 (ESI sec. 6.1)** together with additional discussion on the fit results. Notably, the fit returned percentages of ca. 70 % and 30 % over total Cu for Zr-Cu and Zr-His-Cu species, respectively within the His-Cu-1 sample, which proved to be consistent with the post-synthesis compositional data reported in Table 1.

In summary, His-Cu-2 can be predominantly described by the Zr-Cu model (see Fig. 2B), whereas His-Cu-1 comprises additionally a minor fraction of Zr-His-Cu species (see Fig. 2C). Given that the synthesis procedure was analogous for both examined samples, the quantity of histidine thus plays the main role in differentiating spectroscopically the two samples, as evidenced both qualitatively and quantitatively by XANES and EXAFS analysis.

2.5. Infra-red (IR) spectroscopy

The effect of histidine and copper insertion has been monitored by IR spectroscopy, following the spectra evolution in the OH region, upon thermal treatment in vacuo at 150 °C for 90 min (Fig. 5A). The IR spectrum of parent UiO-66 (black curve) is characterized by a single main component at 3674 cm^{-1} tailed on the low-frequency side, associated to the ν(O–H) stretching of isolated μ$_3$–OH species on the cornerstones of the Zr_6-cluster of the MOFs [48,53–55]. The effect of histidine insertion (blue and light blue curves) implies the appearance of two new absorptions, one at the high (3685 cm^{-1}) and one at the low (3625 cm^{-1}) frequency side of the main band at 3674 cm^{-1} that, at the same time decreases in intensity. The component at 3685 cm^{-1} can be explained by ν(O–H) of μ$_3$–OH, interacting with the nitrogen atom of histidine, while the component at 3625 cm^{-1} implies the presence of some hydrogen-bonded OH species, most probably μ$_3$–OH or OH on defects, interacting with the α-NH_2 group of histidine, as suggested by the computational models in Fig. 2. When copper is added (red and magenta curves) the component at 3685 cm^{-1} is eroded, suggesting a new arrangement of histidine, now interacting with copper, in parallel the main component at 3674 cm^{-1} gains again in intensity, and a new band at 3650 cm^{-1}, possibly associated to Cu-OH, appears.

CO adsorption at Liquid Nitrogen Temperature (LNT) monitored by FT-IR spectroscopy was performed for a qualitative evaluation of the species present in the materials pre-treated for 90 min at 150 °C in a dynamic vacuum. The open metal sites accessible interact differently with CO causing shifts of the CO band compared to the condensed phase (liquid-like component at 2133 cm^{-1}), resulting in the appearance of many components [56]. From Fig. 5B-F we report the sequence of spectra (in subtraction from the activated sample profile) from high to low CO coverages; in all cases, the highest coverage is reported in the same color as the spectrum of the corresponding sample reported in Fig. 5A, while all the other spectra are reported in gray. At very high coverages the spectra are dominated by the effect of the gas: roto-vibrational contributions and typical waves on the high and low sides of the main band at 2133 cm^{-1}. To identify more easily the specific components due to CO interacting with the Brønsted and Lewis sites, it is better to consider the spectra collected at lower coverages (gray curves). Fig. 5B illustrates the sequence of decreasing CO coverages, obtained in the case of parent UiO-66. The main components are observed at 2178 cm^{-1}, associated with CO interacting with Zr cations, at 2153 cm^{-1} due to CO interacting with isolated μ$_3$–OH, and at 2133 cm^{-1} ascribed to liquid-like CO. Fig. 5C and D report the effect of CO dosage on histidine functionalized samples. Spectral components are very similar in both cases: bands at 2178 cm^{-1}, associated with CO interacting with Zr cations, at 2153 cm^{-1} due to CO interacting with isolated μ$_3$–OH (in both samples less intense than what found in the parent UiO-66) and a complex band at 2133 cm^{-1}, ascribed to liquid like CO. Fig. 5E and F illustrate the effect of CO dosage on histidine functionalized samples

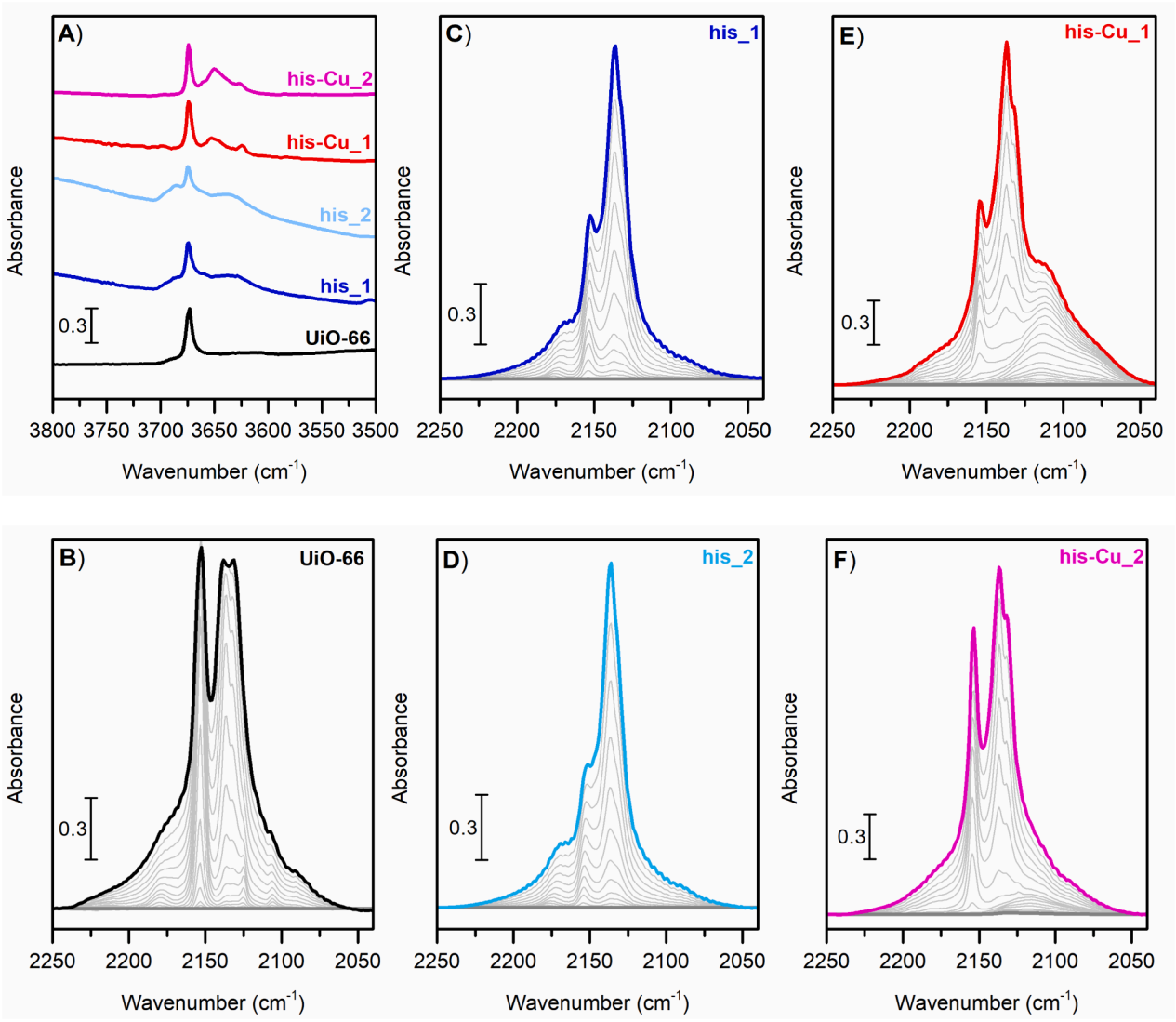

Fig. 5. (A): IR spectra of activated samples (dynamic vacuum at 150 °C for 90 min). (**B**): Effect of CO adsorption at LNT on the parent UiO-66. (**C**): Effect of CO adsorption at LNT on high histidine loaded UiO-66. (**D**): Effect of CO adsorption at LNT on low histidine loaded UiO-66. (**E**): Effect of CO adsorption at LNT on high histidine loaded UiO-66 and successively metalation with copper. (**F**): Effect of CO adsorption at LNT on low histidine loaded UiO-66 and successively metalated.

upon successive metalation. Firstly, the component of CO on the Zr^{4+} cation is not visible anymore (lack of the band at 2178 cm^{-1}), and the component at 2153 cm^{-1} due to CO interacting with isolated μ_3–OH is gaining intensity, as expected looking at the spectra in Fig. 5A, where the components at 3674 cm^{-1} are more intense in these two samples than in those functionalized by histidine. Finally, in both samples, a new component is visible at 2110 cm^{-1}. This band, very broad and most probably composed of more than one component, is more resistant to the outgassing and can be assigned to CO interacting with Cu(I). The intensity of this band is higher in the sample containing more copper. CO interaction is not completely reversible in the case of these two last samples, for which CO is fully desorbed only upon increasing the temperature along outgassing. The formation of some Cu(I) upon mild thermal activation in vacuo was previously observed [54].

Evaluation of the fraction of reduced Cu is not possible, since the values for the attenuation coefficients of Cu-CO adducts are not available. However, we do not expect it to be very pronounced, as the electronic spectra collected in the d-d transition region do not show any significant change for the His-Cu-1 material after activation in vacuum and then repeating the same activation followed by exposure to O_2 atmosphere (see **Supporting Information**, **Figure S21**). A summary of the observed CO-interaction components in the infrared spectra is given in Table 2.

As it was observed that upon activation in vacuum, a portion of Cu (II) is reduced to Cu(I), the two samples with copper were probed again with CO after a mild treatment in oxygen to see the reversibility of the phenomenon. The obtained spectra were very similar to the original ones and only a minor decrease of the bands at 2110 cm^{-1} was observed, without showing any evidence of the formation of Cu(II)–CO adducts. By comparing the CO coverages at 0.2 mbar at low temperatures, this O_2 treatment seems to decrease the intensity of the Cu(I) species, to a greater extent for the sample with more copper (see **Supporting Information Figure S20**). PXRD patterns were registered for the

Table 2
Summary of the main components observed and their assignments.

Band (cm^{-1})	Assignment	UiO-66	His-1	His-2	His-Cu-1	His-Cu-2
2178	Zr…CO	x	x	x		
2153	OH…CO	x	x	x	x	x
2133	Liquid-like CO	x	x	x	x	x
2110	Cu(I)…CO				x	x

pelletized materials after both CO adsorption experiments. They retained their crystallinity in all cases, as displayed in **Figure S22 (ESI)**.

This set of data suggests the presence of a variety of Cu species (in agreement with what was observed in XAS and described in DFT calculations), mostly present as Cu(II) even when the sample is treated under reducing conditions (high vacuum at 150 °C). The reduced species, most probably present as Cu(I), show a coordinative vacancy but do not react extensively with O_2, as testified by the very similar spectrum obtained upon dosing CO.

2.6. Catalytic testing for cyclohexene oxidation in the liquid phase

The synthesized materials were tested for cyclohexene peroxidation with t-BuOOH in Trifluorotoluene at 25 °C, as detailed in the **ESI, Section S7**. During the initial testing, it became clear that the activity of UiO-66-his-Cu varies depending on the pre-treatment of the material, and thus, to ensure comparability across samples, all materials were pre-treated in vacuum for 1 h at 150 °C. This treatment removes undesired adsorbates, and the temperature and time chosen mirrored those used for the pre-treatment to measure the surface area, ensuring that the conditions are not too harsh to lead to pore collapse. Fig. 6A shows a typical reaction involving the UiO-66-his-Cu catalyst. Note that both the substrate and the products are continuously consumed and formed, respectively. However, the total mass balance seems not to be closed, with a total of 30 mM substrate being consumed and only 10 mM products being formed. We also analyzed the gas phase, finding that only a small fraction of CO_2 is formed (ca. 0.003 %) suggesting no significant overoxidation. Instead, it is the volatility of the substrate causing the open mass balance. We determined the Henry's constant for cyclohexene in the solvent (0.003 mol Pa/m^3) and were then able to account for the substrate partitioning between the liquid and gas phases. By continuous sampling, the gas phase expands, lowering the partial pressure of cyclohexene and thus also lowering the concentration in the liquid phase, which can be calculated, resulting in the concentrations reported in Fig. 6. It is clear that, within some approximation, the change in substrate can be traced back to this liquid/gas partitioning. On the other hand, the vapor pressure of the products is fairly low allowing us to follow their formation rate, which is equal to the consumption rate of the substrate, granted that no other side products are formed, or that overoxidation rates of the product are fairly slow (**Supplementary Information**, **Figure S23**).

2.6.1. The role of Cu in cyclohexene oxidation

The above results highlight the formation of products when exposed to the Cu-catalyst. However, several control experiments needed to be performed to ascribe this activity to the Cu in the metal–organic framework (Fig. 6B). As discussed above, we only follow the oxygenated product yields with Table 3 listing the product formation for various reaction conditions. In the absence of the t-BuOOH oxidant, the Cu-catalyst is not able to transform cyclohexene into oxygenated products (<0.1 % yield). Use of the oxidant alone achieves only a slightly higher yield of 0.5 % after 96 h. In the presence of a Cu-free MOF, a comparable, negligible yield is achieved suggesting that the MOF itself does not contribute to the oxidation of the substrate. Thus, it is only the combination of Cu and the peroxide that yields a noticeable amount of products, as is the case for both homogeneous Cu ions and Cu hosted in UiO-66-his. The rate of formation appears to be twice as high for the Cu sites hosted in the MOF than those in solution, highlighting the role confinement of the Cu species plays in transforming the substrate.

2.6.2. Comparing different UiO-66-his-Cu batches

With the Cu-MOF exhibiting an outstanding performance compared to homogeneous systems, we now set out to compare the various batches synthesized (Table 3). Note that a third batch (His-Cu-3; see Table 1) was prepared following a comparable but alcohol-free synthesis route, ensuring that a sufficient supply of catalyst was available. According to the advanced characterization, both the high Cu/his and low Cu/his samples have a significant contribution of Cu interacting with the zirconia nodes allowing us to deduce a similar behavior for the alcohol-free batch. This is further supported by all three batches having comparable reaction profiles following a first-order reaction rate. Therefore, we investigated additional reaction parameters focusing on the alcohol-free sample. We also define the catalytic turnover number (TON) as the number of moles of oxygenate formed relative to the number of moles contained within the catalyst. It is evident from Table 3 that all three batches have comparable TON.

Table 3
The reaction conditions, namely molar ratios as well as the catalyst and reaction outcome are listed. The yields are reported for the end of the reaction at ca. 96 h.

Reaction condition (Cu: substrate: oxidant)	Catalyst	Cu (μmol/g)	Yield (%)	Turnover number (TON)
1: 400: 60	His-Cu-2	362	2.33	10.4
1: 400: 60	His-Cu-1	515	2.0	8.36
1: 400: 60	His-Cu-3	490	2.6	10.5
1: 400: 0	His-Cu-3	490	0.08	0.36
0: 400: 60	No catalyst	n/a	0.4	–
1: 400: 60	UiO-66-$his_{0.42}$	n/a	0.7	–
1: 400: 60	Cu $(BF_4)_2{\cdot}xH_2O$	2682	0.7	3.98

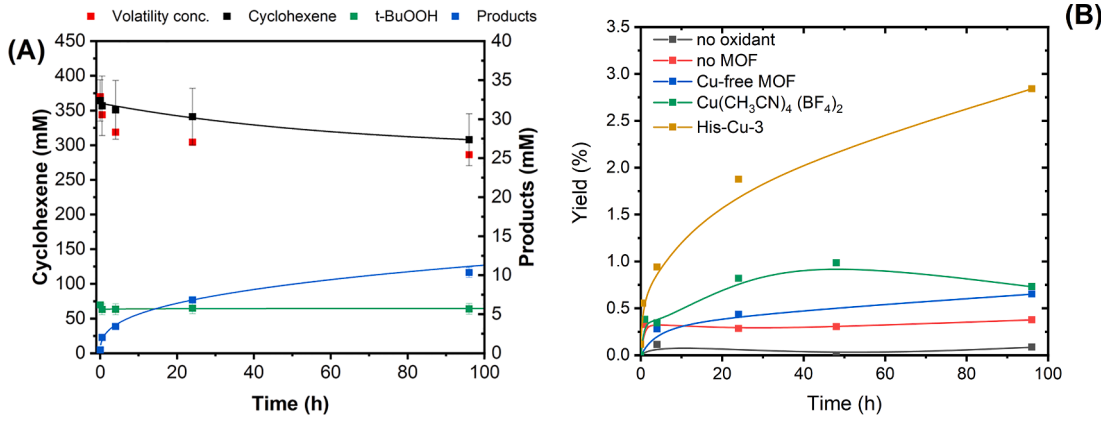

Fig. 6. **(A)**: Concentration profile for cyclohexene and the products formed as a function of the time. The data points were fitted with a first-order rate equation. **(B):** Observed yields for various set of catalyst combinations to determine the active species for the reaction.

2.6.3. Optimizing reaction conditions

The turnover number is a useful descriptor for the stability of the material and the degree of utilization of copper. For example, a material of low stability will quickly deactivate and achieve only a low turnover number. By itself, the turnover number does not indicate anything with regard to catalytic rates or deactivation rates and is only used as a measure of how many molecules can be converted. We notice that very high turnover numbers can be achieved using less Cu catalyst (Fig. 7A). The TON doubles when using only half the Cu and increases by an order of magnitude when using 1/10th of the original Cu content. The TON is measured in all cases after 96 h. The reaction was performed by reducing the amount of Cu while keeping all other parameters the same. There are several explanations for this behavior. Firstly, the yields for the various UiO-66-his-Cu loads appeared to be similar, and Fig. 7B shows yields close to 3 % for both the 0.5 mM and 1 mM Cu loading. In that sense, we are not using all of the Cu effectively which could be due to diffusion limitations (mass transport limited regime) and/or due to strong adsorption of product molecules on the active site blocking further reactions. This would also explain the first-order deactivation behavior. We, therefore, performed the reaction in a bigger vessel with more vigorous stirring while also lowering the Cu loading further (0.1 mM), and this increased the turnover number to 150, with the yield being higher despite a lower amount of Cu being used, suggesting that we are indeed influencing the diffusion behavior by varying the agitation speed. Note, the difference in reaction vessels between initial experiments (8 mL closed cap vial with small stir bar at 1000 rpm) and scaled up experiments (25 mL round bottom flask with larger stir bar at 300 rpm) precludes us from making direct comparisons with respect to mass transfer properties. However, doubling the stirring speed from 300 rpm to 600 rpm increased the oxygenate yield from 4.2 % to 5.9 % confirming the presence of external mass transfer limitations when stirring speeds are low. All subsequent experiments were then performed at 400 rpm to minimize mass transfer limitations to the largest extent possible. Lowering the Cu content also automatically increases the oxidant:Cu ratio from 60:1 to 600:1. Concomitantly, the substrate:Cu ratio also increases with the adsorption constants of cyclohexene and t-BuOOH determining the coverage of the active site. When lowering the oxidant concentration along with the Cu concentration, the yield drops drastically, and the reaction profile also appears to follow more of a zero-order reaction rate. This suggests the rate-limiting role of t-BuOOH and how, at low Cu loadings and low oxidant concentration, most of the active site is likely covered by cyclohexene rather than by t-BuOOH. This prompted us to investigate the possibility of radicals playing a role in cyclohexene oxidation. In Fig. 6A the oxidant concentration is listed in addition to that of the substrate. The initial concentration of ca. 70 mM does not follow a first-order reaction profile, with the concentration after 96 h still hovering around 65 ± 8 mM, suggesting an almost unchanged oxidant concentration. ^{1}H NMR also corroborates this negligible oxidation conversion. Intrigued, we then performed an additional experiment in the absence of the cyclohexene substrate, following only the t-BuOOH concentration. While it still follows a first-order reaction profile, the change in concentration is noticeable, achieving 18 % conversion, and even higher conversions at elevated temperatures (**Supporting information**, **Figure S24**). The decomposition of t-BuOOH catalyzed by Cu results in the formation of t-BuOH, which appears to adsorb too strongly on the active site. Similarly, in the presence of the substrate, the oxygenated products are adsorbed on the confined Cu limiting therefore further conversion of the oxidant. This then suggests that the continued formation of product, beyond the consumption of oxidant, is likely related to radical chain reactions, further explaining why all Cu catalysts achieve comparable yields over the same time. The oxidant leading to the formation of cyclohexenol and cyclohexenone then is atmospheric oxygen, as suggested in Scheme 1. It should be noted, however, that the homogeneous Cu salt deviates from these trends, with oxidant being converted (65 %, **Figure S24**). At the same time, the oxygenated yield is lower. Here, the lack of porous confinement results in weaker adverse adsorption of products while also lacking the ability to trap and concentrate the formed radicals likely needed for the product formation.

2.6.4. Further insight into the catalyst behavior and their stability

Leaching studies were performed by filtering the sampling solution collected 4 h into the reaction and allowing the filtrate to react for 24 h before analyzing. If leaching occurs, the yield and TON in the filtrate will be higher than that measured immediately after sampling the 4 h time point. Fig. 8A compares the turnover numbers achieved for the samples measured right away and those undergoing leaching studies. It appears there is some leaching of Cu from the histidine-containing UiO-66 in all cases, with the His-Cu-2 sample (Cu/his: 7) having the largest relative TON increase in the leached solutions (i.e. 3.1 to 6.7). It could suggest that this sample has the highest concentration of Cu ions in the solution, which contributes to the activity as shown for the Cu(II) tetrafluoroborate salt (Fig. 6B). This could be due to the high Cu/histidine ratio with some of the Cu being anchored more loosely in the MOF and as the Cu/his ratio decreases less leaching occurs. However, we must also posit an alternative explanation. We have seen that for cyclohexane oxidation another product formed is cyclohexyl-hydroperoxide which can be reduced to cyclohexanol by adding triphenylphosphine (TPP) [57]. Similarly, we performed this procedure here at the end of the reaction and found an increase in the cyclohexenol concentration at the expense of the cyclohexenone concentration, suggesting the presence of additional products. (Fig. 8A) It is therefore also possible that the TON measured after leaching is the result of these intermediates reacting to more stable products. We analyzed the tested materials with elemental analysis to see to what extent the copper content has changed (Fig. 8B). The copper concentration in the solid was not reduced sufficiently to attribute the turnover numbers of the leached solutions to Cu ions. The results suggest that the activity of the catalysts does indeed derive

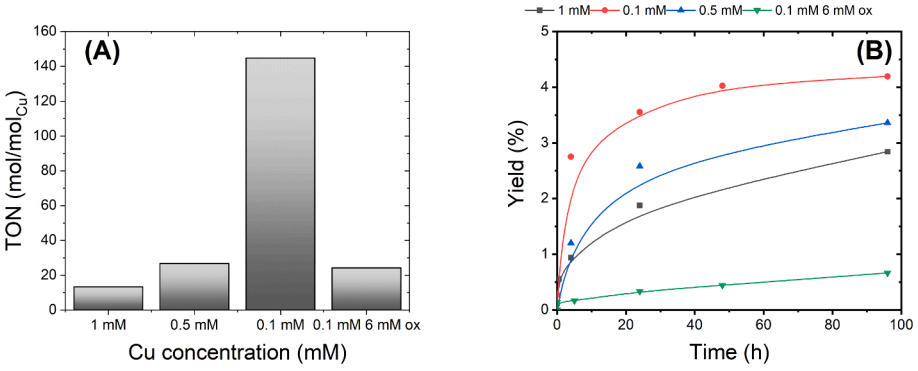

Fig. 7. (**A**) Turnover numbers attained when reducing the Cu loading (and increasing the oxidant: Cu ratio). A turnover number of up to 150 is achieved for 0.1 mM Cu loading. **(B):** Reaction yield as a function of time for the same data set.All tests were performed on His-Cu-3.

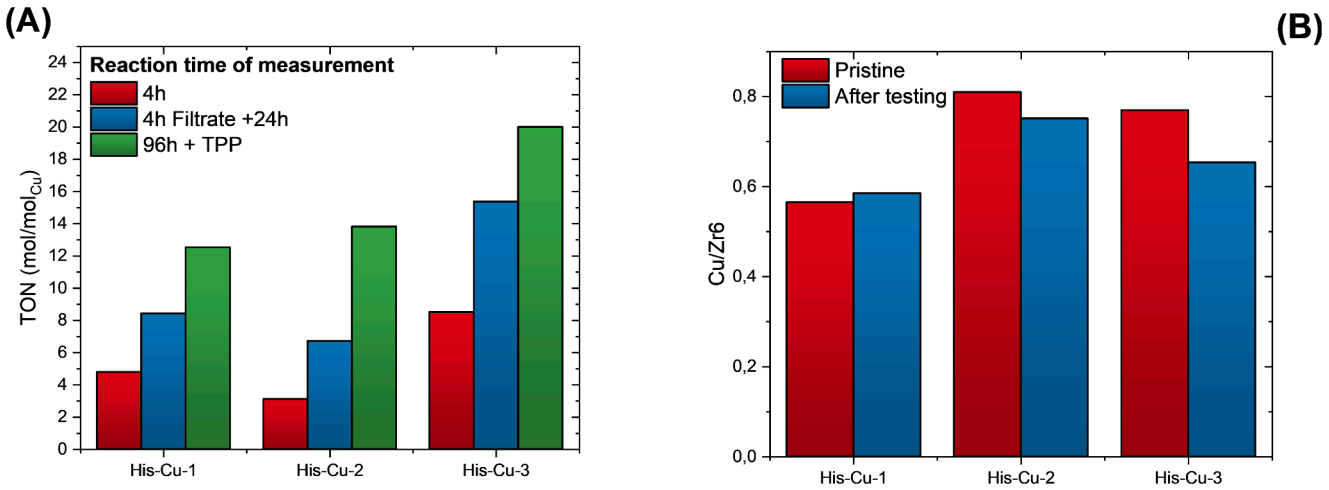

Fig. 8. (A): Turnover numbers (TON) recorded after 4 h of reaction as well as of the filtrate collected after 4 h and allowed to react over 24 h before measurement as a way of assessing Cu species leaching into solution. The TON of the samples containing triphenylphosphine (TPP) was obtained after 96 h, the end of the reaction. **(B):** Cu content of the pristine and tested MOFs.

primarily from Cu anchored inside the MOF. The samples also retained their high crystallinity.

2.6.5. *Alternative reaction conditions*

These findings do suggest that the reaction proceeds *via* Cu sites within the metal–organic framework and that the deactivation behavior is likely attributed to some form of product inhibition, such as coordination of oxygenated products or t-BuOH (as a by-product of t-BuOOH activation) on the Cu sites. We therefore investigated some additional reaction parameters, such as alternative oxidants and solvents (Fig. 9). It is clear from this graph that the combination of t-BuOOH and Trifluorotoluene leads to a high initial formation rate followed by reaching a plateau. In contrast, using more coordinating solvents such as acetonitrile or ethanol, a linear behavior is observed. It should be noted that only 2 data points are measured, however, if the trend were to deviate from linearity one would not expect a doubling of the yield at a doubling of the time, as is the case. This trend indicates that the coverage of the active site is possibly accomplished by t-BuOH. Trifluorotoluene is not strong enough to displace the alcohol, in contrast to acetonitrile or ethanol. At the same time, the high polarity of ethanol and the oxophilic nature of the Cu salt can explain the low yield achieved for this combination. Lastly, a deviation from the 1st order reaction rate is also observed when using H_2O_2 in combination with acetonitrile (H_2O_2 is immiscible with Trifluorotoluene). Here we observe a zero-order behavior suggesting full coverage of the active site by the substrate and higher yields, which can be attributed to the stronger oxidizing ability. Consequently, we also measure slightly higher levels of CO_2, although still negligibly small.

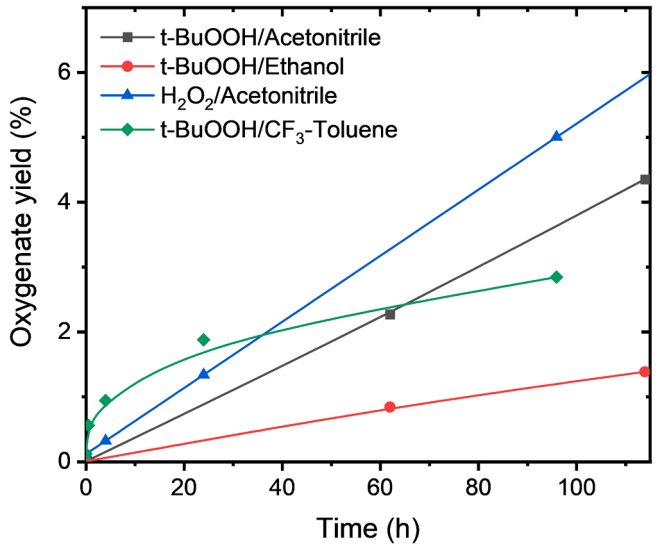

Fig. 9. Testing of His-Cu-3 in various solvents in addition to different oxidants emphasizes the effectiveness of Trifluorotoluene solvent, but also the quick catalyst deactivation in this solvent.

3. Conclusion

In this contribution, a series of UiO-66-his-Cu catalysts with varying histidine and Cu content were synthesized and extensively characterized by XRD, N_2 physisorption, TGA, MP-AES, IR, UV–VIS, XAS, and DFT calculations. Histidine and Cu were incorporated into the MOF materials without significantly impacting their crystallinity or porosity. The catalytic motif of the materials was found to consist mainly of single Cu ions anchored to open node sites. With increasing histidine content, DFT-assisted XAS analysis indicated that a minor fraction of the single Cu ions was anchored to histidine.

Catalytic testing of the three materials showed they possessed similar activity (TON) for the title reaction, in line with the characterization results. Both Cu and the t-BuOOH oxidant were essential for the reaction, indicating that initial radical formation took place at the Cu site. The low conversion of t-BuOOH, however, suggested that O_2 is the main oxidant, and leaching studies indicated a radical chain reaction mechanism, which is in line with prior literature.

Using Trifluorotoluene solvent ensured good solubility of substrate, oxidant, and products and yielded high initial reaction rates but rapid deactivation, which was assigned to competitive sorption of reaction products. A comparison to more polar solvents, acetonitrile and ethanol, showed that the acetonitrile, which has the intermediate polarity of the three, gave the highest oxygenate yield during 100 h of reaction, without deactivation.

Overall, this study highlights the challenges of mimicking the structure and reactivity of enzymes in metal–organic frameworks and the need to perform in-depth characterization and reactivity studies to understand better their correlation.

CRediT authorship contribution statement

Erlend Aunan: Writing – review & editing, Writing – original draft, Visualization, Methodology, Investigation, Formal analysis. **Valeria**

Finelli: Writing – original draft, Investigation. **Sebastian Prodinger:** Writing – review & editing, Writing – original draft, Methodology, Investigation, Formal analysis. **Ning Cao:** Writing – review & editing, Writing – original draft, Investigation, Data curation. **Beatrice Garetto:** Writing – review & editing, Writing – original draft, Investigation, Data curation. **Gabriele Deplano:** Investigation. **Peter Ng'ang'a Njoroge:** Investigation. **Matteo Signorile:** Investigation. **Elisa Borfecchia:** Writing – review & editing, Supervision, Investigation. **Karl Petter Lillerud:** Supervision. **Ainara Nova:** Supervision, Writing – review & editing. **Silvia Bordiga:** Writing – review & editing, Writing – original draft, Supervision, Resources, Project administration, Funding acquisition. **Unni Olsbye:** Writing – review & editing, Writing – original draft, Supervision, Resources, Project administration, Funding acquisition, Conceptualization.

Declaration of competing interest

The authors declare that they have no known competing financial interests or personal relationships that could have appeared to influence the work reported in this paper.

Data availability

Data will be made available on request.

Acknowledgments

This project has received funding from the European Research Council (ERC) under the European Union's Horizon 2020 research and innovation program (grant agreement No 856446 (CUBE)). This work was partly supported by the Research Council of Norway through the Norwegian NMR Package in 1994 and partly supported by the Research Council of Norway through the Norwegian NMR Platform, NNP (226244/F50), as well as The Norwegian Centre for X-ray diffraction, Scattering and Imaging (RECX) (no. NFR 208896/F50). Concerning V. F. activities, this paper and related research have been conducted during and with the support of the Italian national inter-university PhD course in Sustainable Development and Climate change (link: https://www.phd-sdc.it). N.C. and A.N. acknowledge the support from the Research Council of Norway through the Centre of Excellence (No. 262695) and Sigma2 for computational resources (No. nn4654k). V. F., B. G., G. D., M. S., E. B., and S.B. acknowledge support from Project CH4.0 under the MUR program "Dipartimenti di Eccellenza 2023-2027" (CUP: D13C22003520001). We acknowledge the European Synchrotron Radiation facility (ESRF) for provision of synchrotron radiation facilities under proposal number CH-6440 and we would like to thank Cessare Atzori for assistance and support in using beamline BM23.

Appendix A. Supplementary data

Supplementary data to this article can be found online at https://doi.org/10.1016/j.jcat.2024.115722.

References

[1] F.J. Tucci, A.C. Rosenzweig, Direct methane oxidation by copper- and iron-dependent methane monooxygenases, Chem. Rev. 124 (3) (2024) 1288–1320, https://doi.org/10.1021/acs.chemrev.3c00727.
[2] B. Bissaro, V.G.H. Eijsink, Lytic polysaccharide monooxygenases: enzymes for controlled and site-specific fenton-like chemistry, Essays Biochem. 67 (3) (2023) 575–584, https://doi.org/10.1042/EBC20220250.
[3] L.S. Andrade, H.H.L.B. Lima, C.T.P. Silva, W.L.N. Amorim, J.G.R. Poço, A. López-Castillo, M.V. Kirillova, W.A. Carvalho, A.M. Kirillov, D. Mandelli, Metal-organic frameworks as catalysts and biocatalysts for methane oxidation: the current state of the art, Coord. Chem. Rev. 481 (2023) 215042, https://doi.org/10.1016/j.ccr.2023.215042.
[4] S.D. McCann, S.S. Stahl, Copper-catalyzed aerobic oxidations of organic molecules: pathways for two-electron oxidation with a four-electron oxidant and a one-electron redox-active catalyst, Acc. Chem. Res. 48 (6) (2015) 1756–1766, https://doi.org/10.1021/acs.accounts.5b00060.
[5] L. Ciano, G.J. Davies, W.B. Tolman, P.H. Walton, Bracing copper for the catalytic oxidation of C-H bonds, Nat. Catal. 1 (8) (2018) 571–577, https://doi.org/10.1038/s41929-018-0110-9.
[6] R.J. Quinlan, M.D. Sweeney, L. Lo Leggio, H. Otten, J.-C.-N. Poulsen, K. S. Johansen, K.B.R.M. Krogh, C.I. Jørgensen, M. Tovborg, A. Anthonsen, T. Tryfona, C.P. Walter, P. Dupree, F. Xu, G.J. Davies, P.H. Walton, Insights into the oxidative degradation of cellulose by a copper metalloenzyme that exploits biomass components, Proc. Natl. Acad. Sci. 108 (37) (2011) 15079–15084, https://doi.org/10.1073/pnas.1105776108.
[7] B. Ruscic, Active thermochemical tables: sequential bond dissociation enthalpies of methane, ethane, and methanol and the related thermochemistry, J. Phys. Chem. A 119 (28) (2015) 7810–7837, https://doi.org/10.1021/acs.jpca.5b01346.
[8] B. Bissaro, Å.K. Røhr, G. Müller, P. Chylenski, M. Skaugen, Z. Forsberg, S.J. Horn, G. Vaaje-Kolstad, V.G.H. Eijsink, Oxidative cleavage of polysaccharides by monocopper enzymes depends on H2O2, Nat. Chem. Biol. 13 (10) (2017) 1123–1128, https://doi.org/10.1038/nchembio.2470.
[9] R. Kont, B. Bissaro, V.G.H. Eijsink, P. Väljamäe, Kinetic insights into the peroxygenase activity of cellulose-active Lytic Polysaccharide Monooxygenases (LPMOs), Nat. Commun. 11 (1) (2020) 5786, https://doi.org/10.1038/s41467-020-19561-8.
[10] M. Gudmundsson, S. Kim, M. Wu, T. Ishida, M.H. Momeni, G. Vaaje-Kolstad, D. Lundberg, A. Royant, J. Ståhlberg, V.G.H. Eijsink, G.T. Beckham, M. Sandgren, Structural and electronic snapshots during the transition from a Cu(II) to Cu(I) metal center of a lytic polysaccharide monooxygenase by X-Ray photoreduction*, J. Biol. Chem. 289 (27) (2014) 18782–18792, https://doi.org/10.1074/jbc.M114.563494.
[11] S.M. Mahajani, M.M. Sharma, T. Sridhar, Uncatalysed oxidation of cyclohexene, Chem. Eng. Sci. 54 (18) (1999) 3967–3976, https://doi.org/10.1016/S0009-2509(99)00095-0.
[12] Z. Tian, A. Fattahi, L. Lis, S.R. Kass, Cycloalkane and cycloalkene C−H bond dissociation energies, J. Am. Chem. Soc. 128 (51) (2006) 17087–17092, https://doi.org/10.1021/ja065348u.
[13] S.-I. Imamura, T. Banba, Y. Takegami, Liquid-phase oxidation catalyzed by Cu(II)–Cl system, I. Oxidation of cyclohexene, Bull. Chem. Soc. Jpn. 46 (3) (1973) 856–860, https://doi.org/10.1246/bcsj.46.856.
[14] B.M. Weckhuysen, A.A. Verberckmoes, I.P. Vannijvel, J.A. Pelgrims, P.L. Buskens, P.A. Jacobs, R.A. Schoonheydt, Zeolite encaged Cu(Histidine) complexes as mimics of natural Cu enzymes, Angew. Chemie Int. Ed. English 34 (23–24) (1996) 2652–2654, https://doi.org/10.1002/anie.199526521.
[15] B.M. Weckhuysen, A.A. Verberckmoes, L. Fu, R.A. Schoonheydt, Zeolite-encapsulated copper(II) amino acid complexes: synthesis, spectroscopy, and catalysis, J. Phys. Chem. 100 (22) (1996) 9456–9461, https://doi.org/10.1021/jp953684j.
[16] D. Jiang, T. Mallat, D.M. Meier, A. Urakawa, A. Baiker, Copper metal-organic framework: structure and activity in the allylic oxidation of cyclohexene with molecular oxygen, J. Catal. 270 (1) (2010) 26–33, https://doi.org/10.1016/j.jcat.2009.12.002.
[17] P. Aguirre, K. Brown, D. Venegas-Yazigi, V. Paredes-García, E. Spodine, [Cu(H2btec)(Bipy)]∞: reusable metal organic polymer catalyst for epoxidation reactions, Macromol. Symp. 304 (1) (2011) 65–71, https://doi.org/10.1002/masy.201150609.
[18] M. Nandi, P. Roy, H. Uyama, A. Bhaumik, Functionalized mesoporous silica supported copper(II) and nickel(II) catalysts for liquid phase oxidation of olefins, Dalt. Trans. 40 (46) (2011) 12510–12518, https://doi.org/10.1039/C1DT10157A.
[19] D. Ruano, M. Díaz-García, A. Alfayate, M. Sánchez-Sánchez, Nanocrystalline M-MOF-74 as heterogeneous catalysts in the oxidation of cyclohexene: correlation of the activity and redox potential, ChemCatChem 7 (4) (2015) 674–681, https://doi.org/10.1002/cctc.201402927.
[20] K. Brown, S. Zolezzi, P. Aguirre, D. Venegas-Yazigi, V. Paredes-García, R. Baggio, M.A. Novak, E. Spodine, [Cu(H2btec)(Bipy)]∞: a novel metal organic framework (MOF) as heterogeneous catalyst for the oxidation of olefins, Dalt. Trans. 8 (2009) 1422–1427, https://doi.org/10.1039/B810414J.
[21] M.R. Maurya, A. Arya, P. Adão, J.C. Pessoa, Immobilisation of oxovanadium(IV), dioxomolybdenum(VI) and copper(II) complexes on polymers for the oxidation of styrene, cyclohexene and ethylbenzene, Appl. Catal. A Gen. 351 (2) (2008) 239–252, https://doi.org/10.1016/j.apcata.2008.09.021.
[22] P. Roy, M. Nandi, M. Manassero, M. Riccó, M. Mazzani, A. Bhaumik, P. Banerjee, Four M4-oxo-bridged copper(Ii) complexes: magnetic properties and catalytic applications in liquid phase partial oxidation reactions, Dalt. Trans. 43 (2009) 9543–9554, https://doi.org/10.1039/B913556A.
[23] K. Vassilev, S. Turmanova, M. Dimitrova, S. Boneva, Poly(Propylene Imine) dendrimer complexes as catalysts for oxidation of alkenes, Eur. Polym. J. 45 (8) (2009) 2269–2278, https://doi.org/10.1016/j.eurpolymj.2009.05.012.
[24] N. Malumbazo, S.F. Mapolie, Silica immobilized salicylaldimine Cu(II) and Co(II) complexes as catalysts in cyclohexene oxidation: a comparative study of support effects, J. Mol. Catal. A Chem. 312 (1) (2009) 70–77, https://doi.org/10.1016/j.molcata.2009.07.006.
[25] A. Ray, D. Maity, A. Pramanik, K.K. Das, M. Nandi, A. Bhaumik, M. Nethaji, S. Mondal, M. Mukherjee, M. Ali, Two highly unsymmetrical tetradentate (N3O) Schiff base copper(II) complexes: template synthesis, structural characterization, magnetic and computational studies, Polyhedron 28 (17) (2009) 3659–3666, https://doi.org/10.1016/j.poly.2009.06.060.
[26] A.N. Zakharov, N.S. Zefirov, Catalytic behavior of copper(II) chelate complexes sterically held in zeolite large cavities and fixed on its outer surface by a

topological anchor, Russ. J. Gen. Chem. 79 (12) (2009) 2563–2573, https://doi.org/10.1134/S1070363209120019.
[27] M. Islam, P. Mondal, S. Mondal, S. Mukherjee, A.S. Roy, M. Mubarak, M. Paul, Use of a new polymer anchored Cu(II) Azo complex catalyst for the efficient liquid phase oxidation reactions, J. Inorg. Organomet. Polym. Mater. 20 (1) (2010) 87–96, https://doi.org/10.1007/s10904-009-9310-8.
[28] P. Cancino, V. Paredes-García, C. Aliaga, P. Aguirre, D. Aravena, E. Spodine, Influence of the lanthanide(Iii) Ion in {[Cu3Ln2(Oda)6(H2O)6]·nH2O}n (LnIII: La, Gd, Yb) catalysts on the heterogeneous oxidation of olefins, Catal. Sci. Technol. 7 (1) (2017) 231–242, https://doi.org/10.1039/C6CY02115H.
[29] S. Parashar, S. Khare, Supported transition metal catalysts of Cu(II), Mn(II) and Co (II): synthesis, characterization, and catalytic behavior, React. Kinet. Mech. Catal. 127 (1) (2019) 469–488, https://doi.org/10.1007/s11144-019-01559-z.
[30] P. Cancino, V. Paredes-García, P. Aguirre, E. Spodine, A reusable cuii based metal-organic framework as a catalyst for the oxidation of olefins, Catal. Sci. Technol. 4 (8) (2014) 2599–2607, https://doi.org/10.1039/C4CY00152D.
[31] M.B. Meder, L.H. Gade, Coordination chemistry of 1,3-Bis(2-Pyridylimino)- and 1,3-Bis(2-Thiazolylimino)soindole copper complexes: investigation of their catalytic behavior in oxidation reactions, Eur. J. Inorg. Chem. 2004 (13) (2004) 2716–2722, https://doi.org/10.1002/ejic.200400012.
[32] C.M. Jones, M.J. Burkitt, EPR spin-trapping evidence for the direct, one-electron reduction of tert-butylhydroperoxide to the tert-butoxyl radical by copper(II): paradigm for a previously overlooked reaction in the initiation of lipid peroxidation, J. Am. Chem. Soc. 125 (23) (2003) 6946–6954, https://doi.org/10.1021/ja034416z.
[33] J. Büker, B. Peng, Mechanistic insights into liquid-phase autoxidation of cyclohexene in acetonitrile, Mol. Catal. 525 (2022) 112367, https://doi.org/10.1016/j.mcat.2022.112367.
[34] J. Baek, B. Rungtaweevoranit, X. Pei, M. Park, S.C. Fakra, Y.-S. Liu, R. Matheu, S. A. Alshmimri, S. Alshehri, C.A. Trickett, G.A. Somorjai, O.M. Yaghi, Bioinspired metal-organic framework catalysts for selective methane oxidation to methanol, J. Am. Chem. Soc. 140 (51) (2018) 18208–18216, https://doi.org/10.1021/jacs.8b11525.
[35] F. Ahmadijokani, R. Mohammadkhani, S. Ahmadipouya, A. Shokrgozar, M. Rezakazemi, H. Molavi, T.M. Aminabhavi, M. Arjmand, Superior chemical stability of UiO-66 metal-organic frameworks (MOFs) for selective dye adsorption, Chem. Eng. J. 399 (2020) 125346, https://doi.org/10.1016/j.cej.2020.125346.
[36] C.G. Piscopo, A. Polyzoidis, M. Schwarzer, S. Loebbecke, Stability of UiO-66 under acidic treatment: opportunities and limitations for post-synthetic modifications, Microporous Mesoporous Mater. 208 (2015) 30–35, https://doi.org/10.1016/j.micromeso.2015.01.032.
[37] H. Wu, T. Yildirim, W. Zhou, Exceptional mechanical stability of highly porous zirconium metal-organic framework UiO-66 and its important implications, J. Phys. Chem. Lett. 4 (6) (2013) 925–930, https://doi.org/10.1021/jz4002345.
[38] J.H. Cavka, S. Jakobsen, U. Olsbye, N. Guillou, C. Lamberti, S. Bordiga, K. P. Lillerud, A new zirconium inorganic building brick forming metal organic frameworks with exceptional stability, J. Am. Chem. Soc. 130 (42) (2008) 13850–13851, https://doi.org/10.1021/ja8057953.
[39] G.C. Shearer, J.G. Vitillo, S. Bordiga, S. Svelle, U. Olsbye, K.P. Lillerud, Functionalizing the defects: postsynthetic ligand exchange in the metal organic framework UiO-66, Chem. Mater. 28 (20) (2016) 7190–7193, https://doi.org/10.1021/acs.chemmater.6b02749.
[40] Y. Hu, Y. Mei, B. Lin, X. Du, F. Xu, H. Xie, K. Wang, Y. Zhou, An active and stable multifunctional catalyst with defective UiO-66 as a support for Pd over the continuous catalytic conversion of acetone and hydrogen, RSC Adv. 11 (1) (2021) 48–56, https://doi.org/10.1039/D0RA09217G.
[41] A. Koutsianos, E. Kazimierska, A.R. Barron, M. Taddei, E. Andreoli, A new approach to enhancing the CO2 capture performance of defective UiO-66 via post-synthetic defect exchange, Dalt. Trans. 48 (10) (2019) 3349–3359, https://doi.org/10.1039/C9DT00154A.
[42] H. Lyu, O.-I.-F. Chen, N. Hanikel, M.I. Hossain, R.W. Flaig, X. Pei, A. Amin, M. D. Doherty, R.K. Impastato, T.G. Glover, D.R. Moore, O.M. Yaghi, Carbon dioxide capture chemistry of amino acid functionalized metal-organic frameworks in humid flue gas, J. Am. Chem. Soc. 144 (5) (2022) 2387–2396, https://doi.org/10.1021/jacs.1c13368.
[43] L.Y. Wang, M.S. Lee, A review on the aqueous chemistry of Zr(IV) and Hf(IV) and their separation by solvent extraction, J. Ind. Eng. Chem. 39 (2016) 1–9, https://doi.org/10.1016/j.jiec.2016.06.004.
[44] CLEARFIELD, A. Preparation of Zirconyl Chloride Octahydrate. US3057678A, 1959.
[45] D. Bůžek, J. Demel, K. Lang, Zirconium metal-organic framework UiO-66: stability in an aqueous environment and its relevance for organophosphate degradation, Inorg. Chem. 57 (22) (2018) 14290–14297, https://doi.org/10.1021/acs.inorgchem.8b02360.
[46] M.J. Cliffe, W. Wan, X. Zou, P.A. Chater, A.K. Kleppe, M.G. Tucker, H. Wilhelm, N. P. Funnell, F.X. Coudert, A.L. Goodwin, Correlated defect nanoregions in a metal-organic framework, Nat. Commun. 5 (2014) 1–8, https://doi.org/10.1038/ncomms5176.
[47] G.C. Shearer, S. Chavan, S. Bordiga, S. Svelle, U. Olsbye, K.P. Lillerud, Defect engineering: tuning the porosity and composition of the metal-organic framework UiO-66 via modulated synthesis, Chem. Mater. 28 (11) (2016) 3749–3761, https://doi.org/10.1021/acs.chemmater.6b00602.
[48] S. Chavan, J.G. Vitillo, D. Gianolio, O. Zavorotynska, B. Civalleri, S. Jakobsen, M. H. Nilsen, L. Valenzano, C. Lamberti, K.P. Lillerud, S. Bordiga, H2 storage in isostructural UiO-67 and UiO-66 MOFs, Phys. Chem. Chem. Phys. 14 (5) (2012) 1614–1626, https://doi.org/10.1039/c1cp23434j.
[49] K. Gekko, E. Ohmae, K. Kameyama, T. Takagi, Acetonitrile-protein interactions: amino acid solubility and preferential solvation, Biochim. Biophys. Acta - Protein Struct. Mol. Enzymol. 1387 (1) (1998) 195–205, https://doi.org/10.1016/S0167-4838(98)00121-6.
[50] B. Sarkar, Y. Wigfield, The structure of copper(II)-histidine chelate: the question of the involvement of the imidazole group, J. Biol. Chem. 242 (23) (1967) 5572–5577, https://doi.org/10.1016/S0021-9258(18)99395-6.
[51] D.K. Sannes, S. Øien-Ødegaard, E. Aunan, A. Nova, U. Olsbye, Quantification of linker defects in UiO-type metal-organic frameworks, Chem. Mater. (2023), https://doi.org/10.1021/acs.chemmater.2c03744.
[52] J. Ye, J.K. Johnson, Design of Lewis pair-functionalized metal organic frameworks for CO2 hydrogenation, ACS Catal. 5 (5) (2015) 2921–2928, https://doi.org/10.1021/acscatal.5b00396.
[53] G.C. Shearer, S. Forselv, S. Chavan, S. Bordiga, K. Mathisen, M. Bjørgen, S. Svelle, K.P. Lillerud, In situ infrared spectroscopic and gravimetric characterisation of the solvent removal and dehydroxylation of the metal organic frameworks UiO-66 and UiO-67, Top. Catal. 56 (9) (2013) 770–782, https://doi.org/10.1007/s11244-013-0027-0.
[54] L. Braglia, E. Borfecchia, L. Maddalena, S. Øien, K.A. Lomachenko, A.L. Bugaev, S. Bordiga, A.V. Soldatov, K.P. Lillerud, C. Lamberti, Exploring structure and reactivity of Cu sites in functionalized UiO-67 MOFs, Catal. Today 283 (2017) 89–103, https://doi.org/10.1016/j.cattod.2016.02.039.
[55] A.D. Wiersum, E. Soubeyrand-Lenoir, Q. Yang, B. Moulin, V. Guillerm, M. Ben Yahia, S. Bourrelly, A. Vimont, S. Miller, C. Vagner, M. Daturi, G. Clet, C. Serre, G. Maurin, P.L. Llewellyn, An evaluation of UiO-66 for gas-based applications, Chem. – an Asian J. 6 (12) (2011) 3270–3280, https://doi.org/10.1002/asia.201100201.
[56] C. Lamberti, A. Zecchina, E. Groppo, S. Bordiga, Probing the surfaces of heterogeneous catalysts by in situ IR spectroscopy, Chem. Soc. Rev. 39 (12) (2010) 4951–5001, https://doi.org/10.1039/C0CS00117A.
[57] G.B. Shul'pin, Metal-catalyzed hydrocarbon oxygenations in solutions: the dramatic role of additives: a review, J. Mol. Catal. A Chem. 189 (1) (2002) 39–66, https://doi.org/10.1016/S1381-1169(02)00196-6.